Supporting Information

Additional Methodological Detail

The circulation reconstruction is not generally optimally based on a single, "nearest-neighbor" analog, which runs a strong risk of leaving out skill-enhancing information from the other near-neighbor analogs (1). We estimated an optimizing number of analogs based on analysis of minimum RMSE in self-reconstruction (reconstruction of model sea level pressure (SLP) in the northeastern Pacific and adjacent North America driven by the same predictor variables as simulated within the model), across the thirty nearest potential analogs. In this analysis the target year is excluded from the pool of possible analogs; otherwise the target year would be identified as an analog of itself, biasing skill evaluation towards unrealistically high values. The mean of the closest 10 analog years was selected by this process and computed as the analog state for each climatological winter (optimizing performance was similar across the 10 to 20 closest analogs). The multivariate Euclidean distance metric (2, 3) was used to characterize the relative closeness of the model and paleoclimatic states for the three predictor variables for each year. The squared chord distance metric was also evaluated since it has shown optimizing properties in other analog-based paleoclimatic reconstruction processes (1, 2), but it performed similarly to the Euclidian metric and the latter was utilized in this study (3).

The period covered by the reconstruction is dictated by the common period of the three gridded predictor data sets, 1571-1977. To independently evaluate the skill of the reconstructions, they were re-gridded to the native grid of the 20th Century Reanalysis v2 (20CR) (4) and compared to the 20CR during the period of overlap for which the reanalysis is the strongest, 1930-1977 (Figs. S5, S6)*. This skill was evaluated in a sequential manner. First, the North American Drought Atlas (NADA) (5) was utilized as predictor, based on the observation that reconstructed summer soil moisture is strongly related to antecedent winter moisture delivery south and west of a line connecting the northwestern United States to northeastern Mexico (6). Employing these NADA grid cells as predictors produced reasonable reconstructions of winter SLP and 200 hPa geopotential height (GPH) in the northeastern Pacific and adjacent North America in comparison to the 20CR. Reconstruction capability was enhanced by employing the gridded FM temperature reconstruction as an additional predictor, over the western North American region 105-130° W/30-55° N (7) (Figs. S5a,c, S6a,c). Further field skill was added by including gridded water year precipitation reconstructions for the region of CA and western Nevada in the United States (CANV) (8, 9) with the NADA and FM temperature predictors; the gain in 200 hPa GPH field skill is particularly notable (Figs. S5c,d, S6c,d). These results are for the MPI-ESM-P model, which is the primary simulation platform utilized here. Corresponding results for the NCAR-CCSM4 and GISS-E2-R models are shown in Figs. S5e-h/S6e-h and Figs. S5i-l/S6i-l respectively (see *Earth System Model Selection and Evaluation* section below).

* In Figure S6 it is important to note that the squared residuals from the 20CR values involved in the CE metric calculations (23) reflect not only each reconstruction's differences from the 20CR per se, but also secondarily encode differences in overall variability between the climate models used for analog selection, which are not necessarily uniform across the spatial domain examined. Thus, while the colored (> 0) CE values shown in Figure S6 indicate skillful explained variability relative to the 20CR mean for each reconstruction individually, the *relative* spatial extent of skill between the reconstructions is more accurately captured by the Pearson's correlation values and significance in Figure S5, since these are independent of differences in overall variability between the climate models.

Since the gridded predictor data sets are derived from western North American tree-ring information that is not independent across the three predictors, there is need to address the issue of potentially problematic predictor overlap. We note that there is no problematic multiple regression multicollinearity in the strict sense, as this involves two or more predictors lying close enough to each other in the *n*-dimension subspace they span to cause large reduction in the precision of one or more estimated regression coefficients formed by projection of the predictand vector into this space (10). In the extreme case of perfect collinearity (multicollinearity) between two (or more) of the predictor vectors, the predictor subspace is strictly reduced by one (or more) dimensions and the variance-covariance matrix of the predictor data is less than full rank and cannot be inverted, causing the estimation of coefficients to fail altogether (10). By construction, the analog reconstruction process does not involve projection of a predictand vector into a predictor subspace. Rather, it evaluates the simple multivariate distance between the predictor vector for a specific year and the correspondingly-defined vectors for the Earth system model years, with the goal of finding a subset of model years closest to the predictor data for a specific year. The optimization of this process is described in the first paragraph above.

Nonetheless, the more general issue of potentially problematic predictor overlap and introduction of redundant information into the analog process remains. We evaluated this by comparing the cross-correlations among all combinations of the regridded predictor data. These values are systematically very small for comparisons of the NADA and FM temperature and FM temperature and CANV precipitation (highest absolute value = 0.35, or $\leq$ 12.25% common variability). In contrast, eight of the eighteen NADA grid cells have generally high correlation with the CANV precipitation cells (typically > 0.707, or > 50% common variability). To determine if these NADA cells add merely superfluous, or even problematic, information to the analog reconstruction process, the reconstruction was redone with them omitted. If the independent skill of this “reduced-NADA” reconstruction was similar to, or even better than, the skill of the original reconstruction, then there is clearly a problem related to predictor overlap and the reduced-NADA reconstruction should be kept. Conversely, if the skill was negatively affected in the reduced-NADA case, then these cells carry important information that should be included in the reconstruction. The results indicate that the omitted NADA information enhances spatial reconstruction skill in the northeastern Pacific and along the western North American coast (Fig S7), and thus the original “full-NADA” reconstruction has been retained.

Earth System Model Selection and Evaluation

The MPI-ESM-P (11), NCAR CCSM4 (12), and GISS-E2-R models (13) were driven by estimations of past changes in solar irradiance, volcanic activity, atmospheric concentrations of greenhouse trace gases, and anthropogenic land-use changes. These simulation platforms were selected for potential use because they each use the same model version for their past-millennium (until 1850), 'historical' (1850-2005), and scenario (into-21st century) simulations, they produce realistic simulated global mean surface temperature, and because they are integrated at high spatial resolution. This combination of characteristics is unique among the CMIP5 model set for last millennium-into-the-21st century simulations. The reconstruction performance of the MPI-ESM-P model is evaluated against the 20CR (4) in Figs. S5a-d/S6a-d, indicating independently validated capability to reconstruct 200 hPa upper tropospheric conditions for a significant portion of the Pacific Ocean (Figs. S5d/S6d), including the entry region of NPJ *u*- and *v*-winds in California. Companion graphics to Fig. S5a-d/S6a-d and Fig. 1a-d for the NCAR CCSM4 model results are provided in Figs. S5e-h/S6e-h and S8, respectively, and for the GISS-E2R model in Fig. S5i-l/S6i-l.

The spatial extent of reconstruction skill assessed against the 20CR is much reduced for the GISS-E2-R model (Figs. S5a-d/S6a-d and S5i-l/S6i-l, note panels S5d/S5l and S6d/S6l), and thus this model was not employed for further analyses. The NCAR CCSM4 model has similarities in skill to that obtained with the MPI-ESM-P model (Figs. S5a-d/S6a-d and S5e-h/S6e-h). However, in contrast to the MPI-ESM-P, the NCAR-CCSM4 skill for the 200 hPa geopotential height field is notably weaker in western North America and not as widely strong in the Pacific Ocean overall (Figs. S5d/S5h and S6d/S6h). Specifically important for the questions examined in this paper, the correlation between CA fire activity and the NCAR-CCSM4-reconstructed NPJwind components is weaker than it is for the MPI-ESM-P model, especially for the *v*-component (Figs. 1b,d and S8b,d), and in turn the NCAR-CCSM4-derived latitudinal profiles of the NPJ *u*- and *v*-wind components in the temperate northeastern Pacific and western North America exhibit little difference between high- and low-fire years in CA (Fig. S9). Based on this information, we also decided not to employ the NCAR-CCSM4 model for further analyses, and utilize the MPI-ESM-P as the primary model evaluation platform.

Model Descriptive Detail

The MPI-ESM-P model is composed of the spectral atmosphere model ECHAM6, with a horizontal resolution of T63 (approximately 1.8 x 1.8 degrees latitude by longitude) with 40 atmospheric levels, and the ocean and sea-ice model MPI-OM, with a horizontal resolution of about 1 x 1 degree latitude by longitude and 40 ocean levels.

The NCAR-CCSM4 atmosphere-ocean model is composed of the finite-difference atmosphere model CAM4, with a horizontal resolution of 0.9 degrees longitude x 1.25 degrees latitude and 26 atmospheric levels, and the Parallel Ocean Program model, with a regular horizontal resolution in the zonal direction of 1.1 degrees and a variable horizontal resolution in the meridional direction between 0.27 degrees at the equator and 0.54 degrees at the subtropics, and approximately constant polewards.

The GISS-E2-R model is composed of the atmospheric model GISS-E2, with a regular horizontal resolution of 2 x 2.5 degrees latitude by longitude and 40 atmospheric levels, and the Russel ocean model with a regular horizontal resolution of 1 x 1.25 latitude by longitude.

All three models were driven by external forcing following protocols recommended by the Intergovernmental Panel on Climate Change (14). The main forcings over the past millennium are volcanic forcing, changes in solar irradiance, greenhouse trace gases, land use changes, and tropospheric aerosols since the onset of the industrial revolution. The prescribed external forcings are, however, not exactly the same for the three models. The volcanic forcing used in the MPI-ESM-P simulations was derived from (15), whereas the volcanic forcing used in the NCAR-CCSM4 and GISS-E2-R simulations was derived from (16). Both volcanic forcing data sets are derived from the pH content in polar ice cores, but are interpreted in slightly different ways. The dating of the volcanic eruptions, identified as pH spikes in the ice core layers, does not always coincide in both data sets, as the two groups sometimes assumed different time lags between an eruption and deposition at the poles. The concentration of greenhouse trace gases is derived from air bubbles trapped in polar ice cores (14). Past changes in solar irradiance were derived by the concentration of cosmogenic isotopes in ice cores, re-scaled to describe changes in Total Solar Irradiance following (17).

Land-use changes were prescribed in the MPI-ESM-P simulations following (18), and in the NCAR-CSM4 and GISS-E2-R simulations merging the reconstructions of (18) and (19).

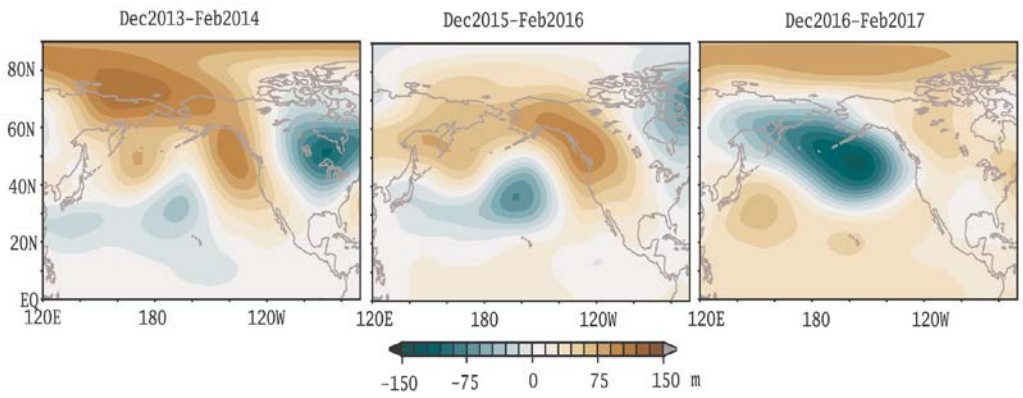

Figure S1. 500 hPa geopotential height anomaly fields (m) in the North Pacific and surrounding regions. For the Northern Hemisphere winters (December-February) of 2013-2014, 2015-2016, and 2016-2017.

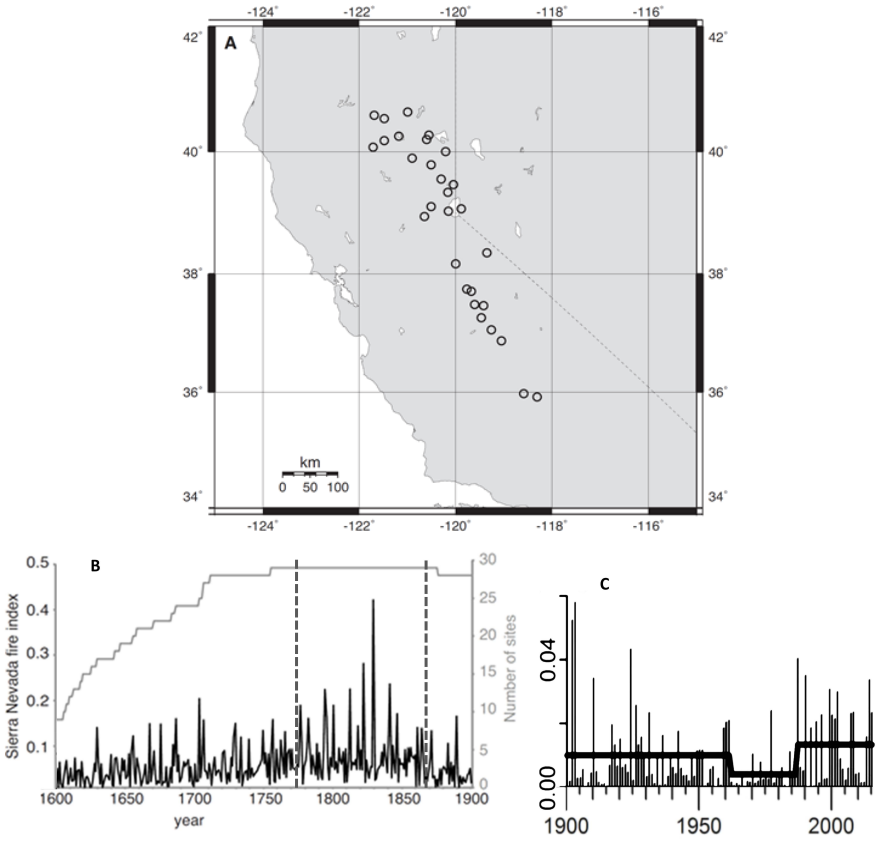

Figure S2. California Fire Index. (20) (a) sites in Sierra Nevada Mountains sampled for fire scar information; (b) time series (1600-1900 CE) of tree scar-based fire index prior to 20th century fire suppression (dark grey line, measured on L-hand vertical axis) and number of sites recording fire (light grey line, measured on R-hand axis), dashed vertical lines denote socio-ecological fire regimes described in primary text; (c) time series of tree scar-based (1900-1907 CE) and documentary-based (1908-2015 CE) fire index during 20th and 21st century period of modern fire suppression (note smaller index values), heavy line indicates relative changes in mean state during this period. [CE is omitted hereafter.]

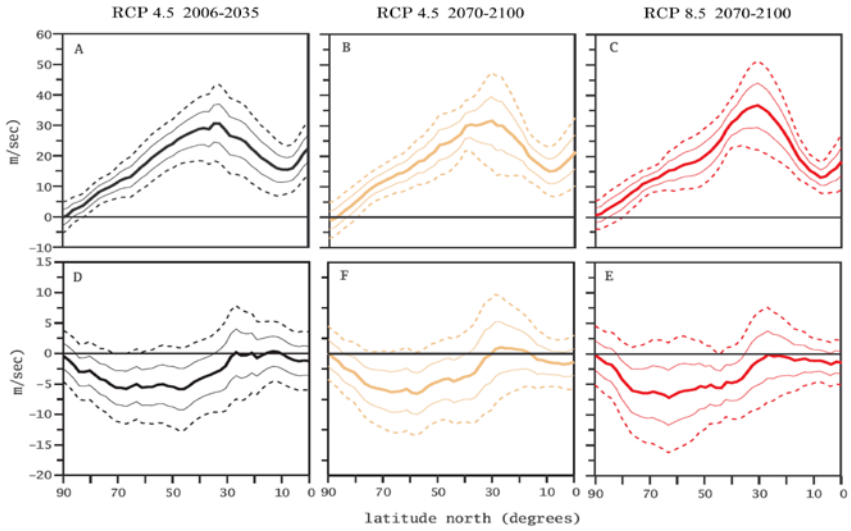

Figure S3. Projected changes in position and intensity of winter North Pacific Jet Stream winds during the 21st century. Latitudinal profiles of winter mean 200 hPa *u*-wind averaged between 120W-130W (a-c) and *v*-wind averaged between 110W-120W (d-f), simulated by the MPI-ESM-P model (11) over three periods in the 21st century, and driven by two scenarios of atmospheric concentration of anthropogenic greenhouse gases according to two Representative Concentration Paths (RCPs) (21): (a, d) under RCP 4.5 over 2006-2035; (b, e) under RCP 4.5 over 2070-2100; (c, f) under RCP 8.5 over 2070-2100. Thick lines indicate mean value at each latitude; thin solid (dashed) lines indicate +-1 (+- 2) times the sample-estimated standard error of the mean.

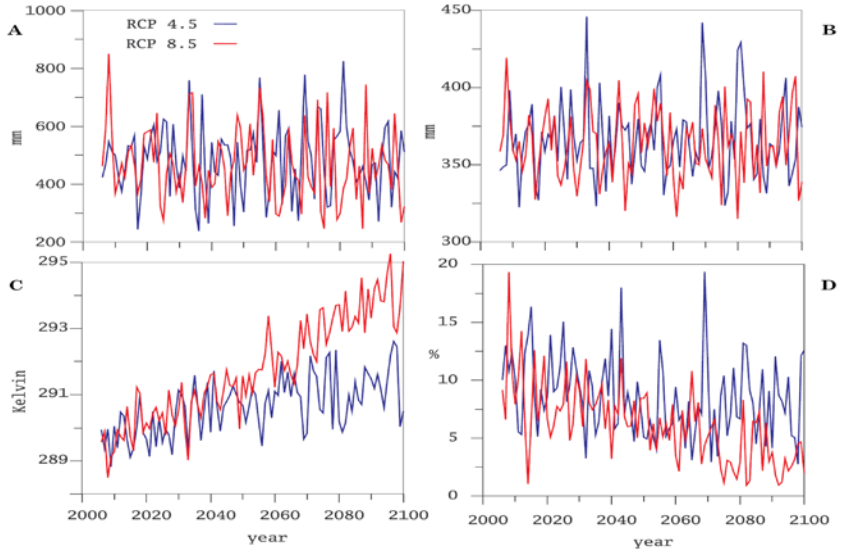

Figure S4. Projected California hydroclimate in the 21st century. Annual California spatial means of (a) precipitation, (b) soil moisture, (c) near-surface air temperature, and (d) percentage of total precipitation occurring as snow, simulated by the MPI-ESM-P model (11), and driven by two scenarios of atmospheric concentration of anthropogenic greenhouse gases according to two Representative Concentration Paths (RCPs) (21): RCP4.5 (blue) and RPC8.5 (red).

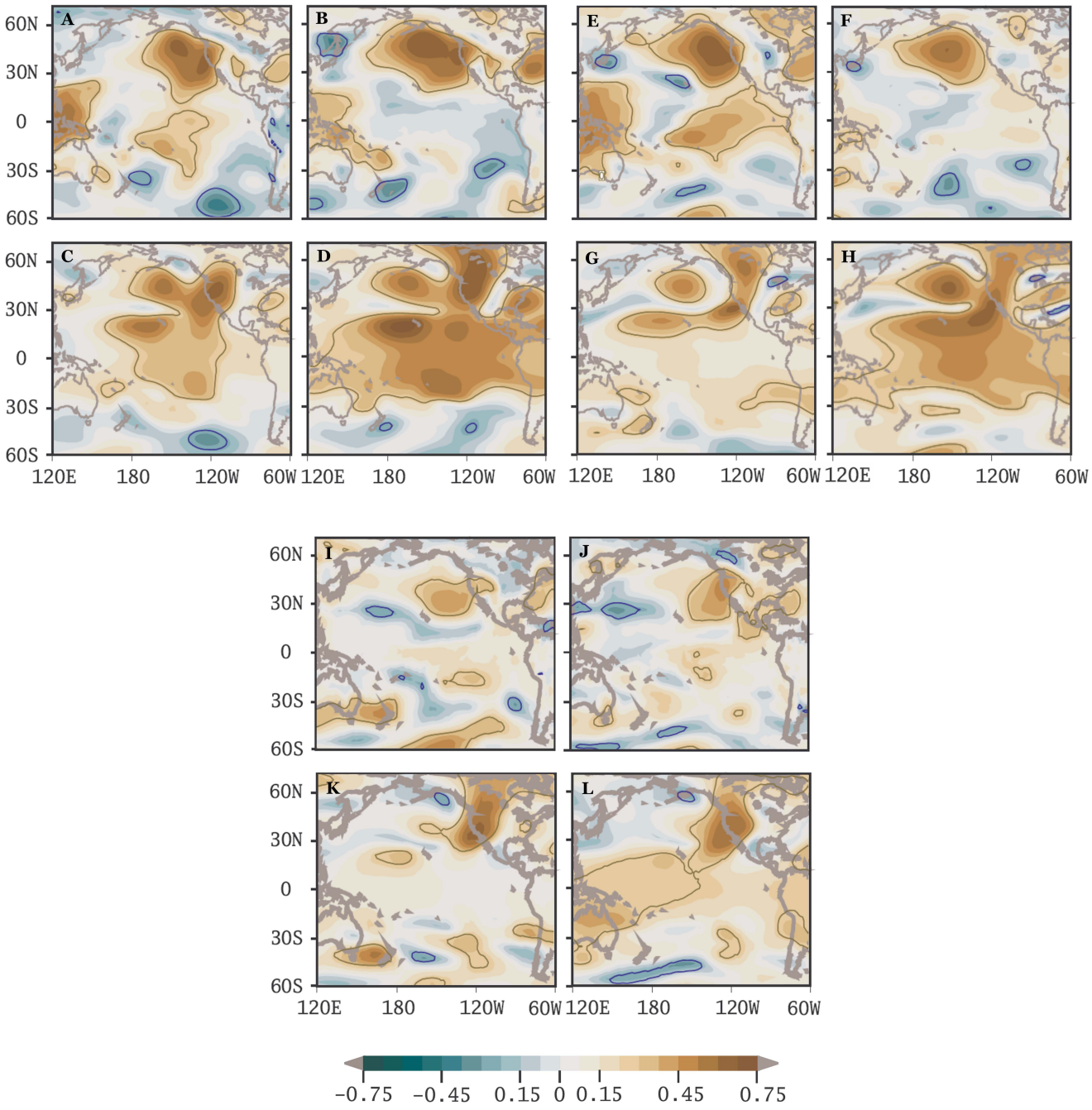

Figure S5. Measures of reconstruction skill of the winter atmospheric circulation. Spatial correlations between the seasonal means (December$_{t-1}$-February$_t$) of the atmospheric fields from the 20CR (4) and their reconstructed counterparts; using the MPI-ESM-P (11) (a-d), NCAR-CCSM4 (12) (e-h), and GISS-E2-R (i-l) (13) models to provide the pool of potential analogs, over the period 1930-1977: (a,e,i) correlation to reconstructed SLP using the NADA and FM temperature as predictors; (b,f,j) correlation to reconstructed SLP using the NADA, FM temperature, and CANV precipitation and as predictors; (c,g,k) correlation to reconstructed 200 hPa geopotential height using the NADA and FM temperature as predictors; (d,h,l) correlation to reconstructed 200 hPa geopotential height using the NADA, FM temperature, and CANV precipitation and as predictors. Contour lines indicate $p < 0.05$ significance levels (brown-positive, blue-negative), corrected for autocorrelation for each grid cell time series (22).

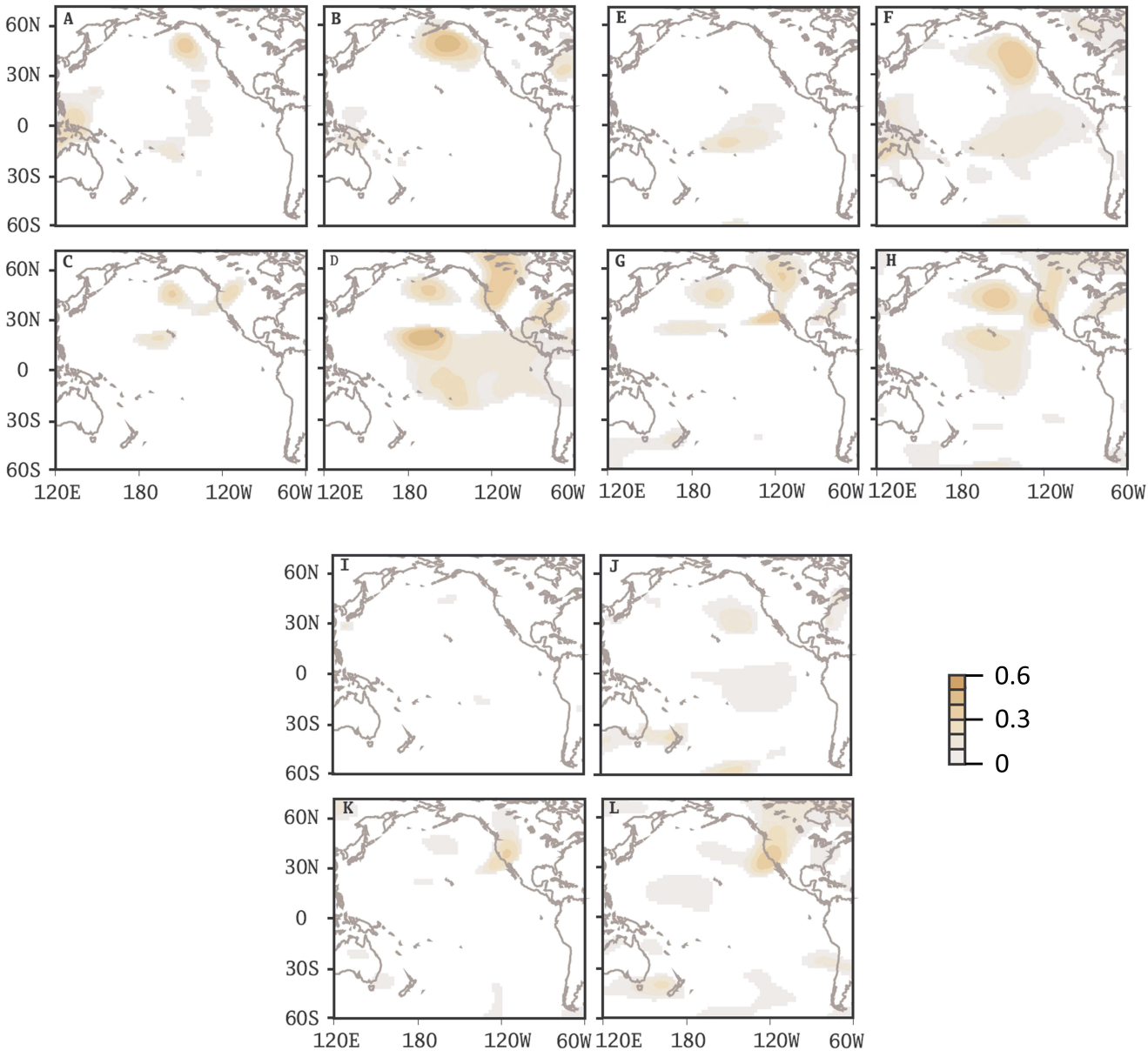

Figure S6. Measures of reconstruction skill of the winter atmospheric circulation. As Figure S5, except that the spatial Coefficient of Efficiency (CE) is shown. There is no analytical significance test for CE, values are reported for regions where CE > 0, indicating reconstruction skill in terms of explained variability relative to the 20CR mean. Note in this case of using an entirely independent data set for the evaluation (i.e., the 20CR is not employed in a reconstruction calibration), CE is numerically identical to the Reduction of Error (RE) and Coefficient of Determination (R^2) metrics (23).

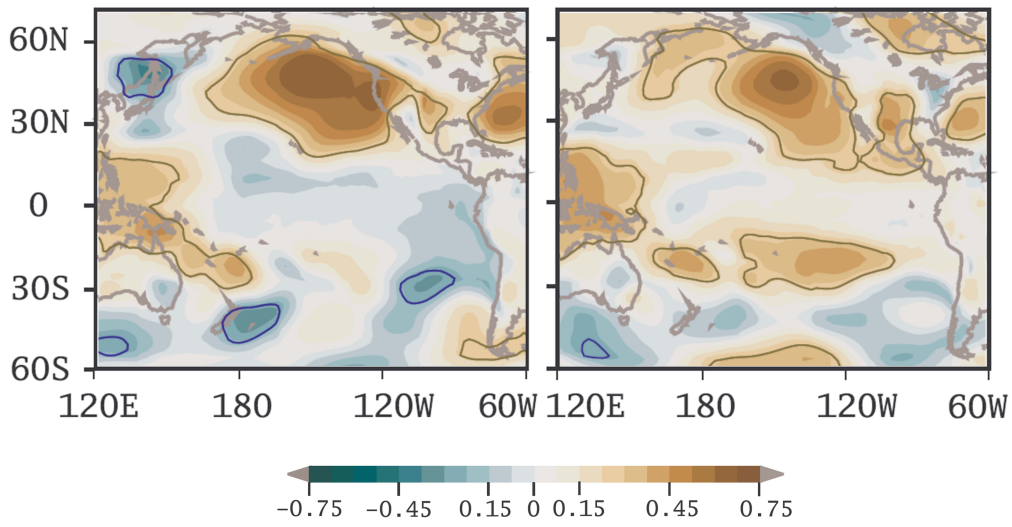

Figure S7. Measures of reconstruction skill of the winter atmospheric circulation. Spatial correlation between the seasonal means (December$_{t-1}$-February$_t$) of the atmospheric SLP from the 20CR (4) and its reconstructed counterpart using the MPI-ESM-P (11); all NADA grid cells retained (left) and eight NADA cells removed that correlate highly with CANV precipitation grid cells (right). Contour lines indicate $p < 0.05$ significance levels (brown-positive, blue-negative), corrected for autocorrelation for each grid cell time series (22).

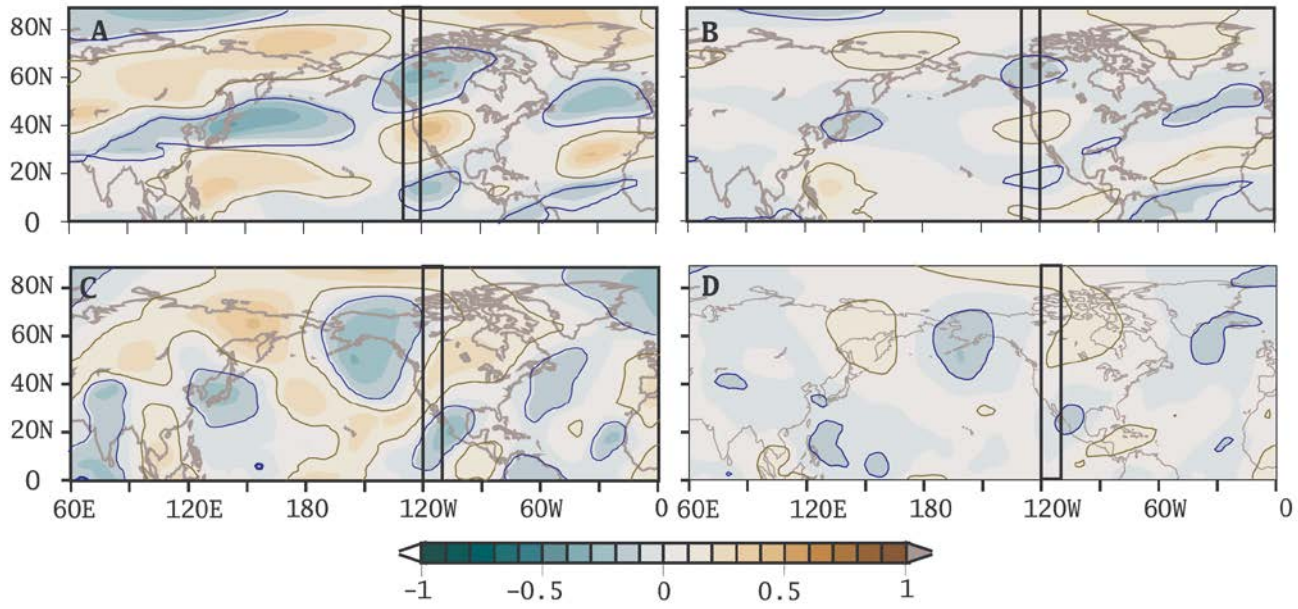

Figure S8. Linkages between winter North Pacific Jet Stream (NPJ) winds and California precipitation and fire activity. As Fig. 1a-d, except NCAR-CCSM4 model (12) is used as analog pool for NPJ wind reconstruction. Contour lines indicate $p < 0.05$ significance levels (brown-positive, blue-negative), corrected for autocorrelation for each grid cell time series (22).

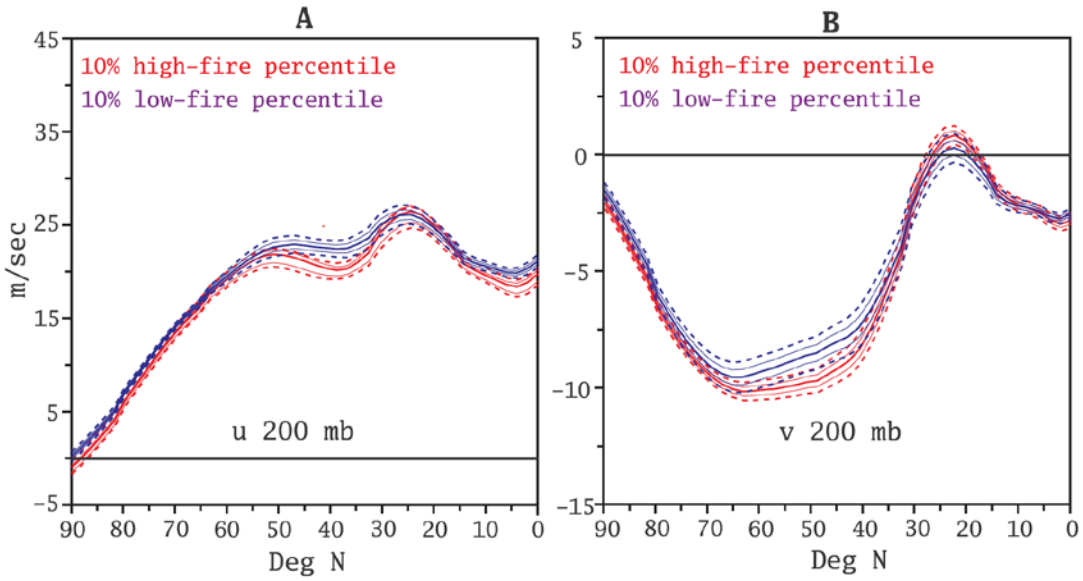

Figure S9. Latitudinal profiles of reconstructed winter North Pacific Jet Stream wind velocity for extreme fire years in California – prior to modern fire suppression. As Fig. 2c-d, except NCAR-CCSM4 model (12) is used as analog pool for NPJ wind reconstruction.

Supporting Information References

1 Wahl ER (2004) A general framework for determining cutoff values to select pollen analogs with dissimilarity metrics in the modern analog technique. *Rev Palaeobot Palyn* 128:263-280.

2 Gavin DG, Oswald WW, Wahl ER, Williams JW (2003) A statistical approach to evaluating distance metrics and analog assignments for pollen records. *Quat Res* 60:356-367.

3 Matulla C, *et al.* (2008) Influence of similarity measures on the performance of the analog method for downscaling daily precipitation. *Clim Dyn* 30:133-144.

4 Compo GP, *et al.* (2011) The Twentieth Century Reanalysis Project. *Quart J Royal Meteorol Soc* 137:1-28.

5 Cook ER, *et al.* (2010) Megadroughts in North America: placing IPCC projections of hydroclimatic change in a long-term palaeoclimate context. *J Quat Sci* 25:48-61.

6 St George S, Meko DM, Cook ER (2010) The seasonality of precipitation signals embedded within the North American Drought Atlas. *Holocene* 20:983-988.

7 Wahl ER, Diaz HF, Smerdon JE, Ammann CM (2014) Late winter temperature response to large tropical volcanic eruptions in temperate western North America: Relationship to ENSO phases. *Glob Plan Change* 122:238-250.

8 Diaz HF, Wahl ER (2015) Recent California Water Year Precipitation Deficits: A 440-Year Perspective. *J Clim* 28: 4637-4652.

9 Wahl E, Diaz H, Vose R, Gross W (2017) Multi-century evaluation of recovery from strong precipitation deficits in California. *J Clim* 30:6053-6063, doi:10.1175/JCLI-D-16-0423.1.

10 Wonnocott RJ, Wonnocott TH (1979) Econometrics, 2nd ed. chap 14. *John Wiley & Sons*.

11 Giorgetta MA, *et al.* (2013) Climate and carbon cycle changes from 1850 to 2100 in MPI-ESM simulations for the Coupled Model Intercomparison Project phase 5. *J Advanc Model Earth Syst* 5:572-597.

12 Landrum L, *et al.* (2013) Last Millennium Climate and Its Variability in CCSM4. *J Clim* 26:1085-1111.

13 Schmidt, GA, *et al.* (2014) Configuration and assessment of the GISS ModelE2 contributions to the CMIP5 archive. *J Adv Model Earth Syst*, 6:141–184, doi:10.1002/2013MS000265.
14 Schmidt GA. *et al.* (2012) Climate forcing reconstructions for use in PMIP simulations of the Last Millennium (v1.1). *Geosci Model Dev* 5:185-191.
15 Crowley TJ, Unterman MB (2013) Technical details concerning development of a 1200 yr proxy index for global volcanism. *Earth Syst Sci Data* 5:187-197.
16 Gao CC, Robock A, Ammann C (2008) Volcanic forcing of climate over the past 1500 years: An improved ice core-based index for climate models. *J Geophys Res Atmos* 113:D23111.
17 Vieira LEA, Solanki SK, Krivova NA, Usoskin I (2011) Evolution of the solar irradiance during the Holocene. *Astron Astrophys* 531:A6.
18 Pongratz J, Reick C, Raddatz T, Claussen MA (2008) Reconstruction of global agricultural areas and land cover for the last millennium. *Glob Biogeochem Cycles* 22:GB3018.
19 Hurtt GC, *et al.* (2009) Harmonisation of global land-use scenarios for the period 1500–2100 for IPCC-AR5. *iLEAPS Newslett* 7:6-8.
20 Taylor AH, Trouet V, Skinner CN, Stephens S (2016) Socioecological transitions trigger fire regime shifts and modulate fire-climate interactions in the Sierra Nevada, USA, 1600-2015 CE. *Proc Natl Acad Sci USA* 113:13684-13689.
21 Van Vuuren DP, *et al.* (2011) The representative concentration pathways: an overview. *Clim Change* 109:5-31.
22 Ebisuzaki W (1997) A method to estimate the statistical significance of a correlation when the data are serially correlated. *J Clim* 10:2147-2153, doi:10.1175/1520 0442(1997)010<2147:AMTETS>2.0.CO;2.
23 Wahl E, Smerdon J (2012) Comparative performance of paleoclimate field and index reconstructions derived from climate proxies and noise-only predictors", *Geophys Res Let*, 39:L06703, doi:10.1029/2012GL051086 (see Supplemental Information, IX).